

# Facile Synthesized Acetamidine Thiocyanate with Synergistic Passivation and Crystallization for Efficient Perovskite Solar Cells

Xinxin Wang, Hao Huang, Shuxian Du, Peng Cui, Zhineng Lan, Yingying Yang, Luyao Yan, Jun Ji, Benyu Liu, Shujie Qu, Qiang Zhang, Xiaopeng Yue, Xing Zhao, and Meicheng Li\*

Further performance enhancement of perovskite solar cells (PSCs) is limited by the defect-assisted recombination losses. The approaches employed to decrease the losses contain defect passivation, perovskite crystallization control, interface engineering, etc. Herein, a new material of acetamidine thiocyanate (AASCN) via a facile method is synthesized, which exhibits dual functions combining a cation with passivation and an anion with crystallization. The iodine vacancies in the perovskite can be effectively passivated through hydrogen bonds formed by the N–H bonds of the polar cation  $AA^+$ . Furthermore, the pseudo-halide anion  $SCN^-$  can coordinate the Pb–I octahedrons, improving the perovskite film crystallization. Through vaporizing the AASCN on perovskite films during the secondary crystal growth process, the defects mitigation and crystallization improvement are synergistically achieved. As a consequence, the  $FA_{0.25}MA_{0.75}PbI_3$  PSCs with AASCN achieve a power conversion efficiency of 23.17%, which is higher than that (21.43%) of untreated PSCs. In detail, the open-circuit voltage has also a significant advancement from 1.095 to 1.167 V after the AASCN treatment. The design and synthesization of the multifunctional materials are supposed to provide a feasible approach for the performance improvement of PSCs.

## 1. Introduction

With the rapid development of power conversion efficiency (PCE) up to 25.7%, perovskite solar cells (PSCs) have been considered a promising photovoltaic technology.<sup>[1–4]</sup> It is reported that the theoretical PCE of PSCs is more than 30%, which suggests that there is still much room for further improvement.<sup>[5]</sup> However, the nonradiative recombination in PSCs has a severe


impact on the open-circuit voltage ( $V_{OC}$ ), which needs to be carefully addressed.<sup>[6]</sup> Deep-level defects in perovskite films are the predominant sources of defect-assisted nonradiative recombination losses.<sup>[7]</sup> Hence, it is necessary to develop an effective strategy to reduce the intrinsic defects including interstitials, vacancies, antisites, and so on.

Defect passivation is considered the most direct approach to boost  $V_{OC}$  and PCE by minimizing nonradiative recombination, which is widely used in the field of PSCs.<sup>[7,8]</sup> The reported works demonstrated that the defect states are mainly located at the surface and interfacial grain boundaries of perovskite films.<sup>[9]</sup> Thus, it is supposed to be an effective method to passivate defects by utilizing appropriate materials as the additive. Organic functional groups such as phenylethylammonium ( $PEA^+$ ), 1,4-butanediammonium ( $BDA^+$ ), and guanidinium ( $GA^+$ ) are widely used for defect passivation in PSCs.<sup>[10–12]</sup> Jiang et al. demonstrated that

PEAI could obtain a higher efficiency device by suppressing nonradiative recombination.<sup>[13]</sup> In PEA materials, the benzene ring  $\pi$ -conjugation structure reduces the neutral iodine related defects, and the amine group forms hydrogen bonds with iodide ions.<sup>[13]</sup> Zhang et al. proposed using  $GA^+$  as a post-treatment reagent, leading to an increase of more than 50% in PCE of quasi-2D PSCs from 8.62% to 13.13%.<sup>[14]</sup> It has been reported that adjusting the polarity of passivation molecules through structural design can effectively improve the adsorption capacity between passivation molecules and defect sites, ensuring passivators fully interact with the defect sites.<sup>[15]</sup> Tan et al. used 4-trifluoromethyl-phenylammonium (CF3-PA) as the passivator, which exhibits a stronger polarity than the widely used PEA, leading to a reliable perovskite surface-passivator interaction.<sup>[16]</sup> Through the improved grain surface passivation with CF3-PA, the PCE of Pb–Sn PSCs and all perovskite tandem solar cell is as high as 22% and 26.4%, respectively.<sup>[16]</sup>

As a type of polycrystalline film, the defect density in perovskite film is closely related to its growth process. Developing an effective crystallization regulation method for

X. Wang, H. Huang, S. Du, P. Cui, Z. Lan, Y. Yang, L. Yan, J. Ji, B. Liu, S. Qu, Q. Zhang, X. Yue, X. Zhao, M. Li  
State Key Laboratory of Alternate Electrical Power System with Renewable Energy Sources  
School of New Energy  
North China Electric Power University  
Beijing 102206, China  
E-mail: mcli@ncepu.edu.cn

 The ORCID identification number(s) for the author(s) of this article can be found under <https://doi.org/10.1002/solr.202200717>.

DOI: 10.1002/solr.202200717

high-quality perovskite films should also be a feasible strategy to reduce the defects and further improve the PCE of PSCs. Anions such as  $\text{COO}^-$  and  $\text{CH}_3\text{COO}^-$  can regulate crystal growth by coordinating with  $\text{Pb}^{2+}$ .<sup>[17,18]</sup> Pseudo-halide anions can augment the crystallinity and suppress anion-vacancy defects of perovskite films.<sup>[18,19]</sup> It is inspired to design a two-in-one functional material that can synergistically realize the passivation by organic polar cations and the crystallization regulation by pseudo-halide anions, providing a simple and feasible approach to minimize nonradiative recombination.

In this article, we proposed a dual-functional material acetamidine thiocyanate (AASCN) to reduce the defects in perovskite films through synergistic defect passivation and crystallization regulation. AASCN includes polar organic cation  $\text{AA}^+$  and pseudo-halide anion  $\text{SCN}^-$ . Among them,  $\text{AA}^+$  has strong chemical bonding with the perovskite to reduce the trap state density, due to the delocalized  $\pi$ -electron cloud over the  $\text{N}-\text{C}-\text{N}$  bond strengthening  $\text{N}-\text{H}\cdots\text{I}$  bond.<sup>[20]</sup> Additionally,  $\text{SCN}^-$  can slow down the crystallization process to obtain dense perovskite films. As a result, the PCE of  $\text{FA}_{0.25}\text{MA}_{0.75}\text{PbI}_3$  PSCs improved from 21.43% to 23.17% with a significant advance in open-circuit voltage from 1.095 to 1.167 V.

## 2. Results and Discussion

AASCN synthesis processes and the photograph of crystalline powder are exhibited in Figure 1a and S1, Supporting Information. To confirm the material molecular structure, Fourier transform infrared (FT-IR) transmission and mass spectrometry were performed with the results shown in Figures S2 and S3, Supporting Information. The FT-IR spectra of AASCN material exhibit the obvious characteristic stretching vibration peaks located at 1660 and 2044  $\text{cm}^{-1}$ , respectively. It is reported

that the peak located at 1660  $\text{cm}^{-1}$  is corresponding to the  $\text{C}=\text{N}$  groups in  $\text{AA}^+$ , and the peak located at 2044  $\text{cm}^{-1}$  is corresponding to the  $-\text{SCN}$  groups.<sup>[21,22]</sup> In addition, we can also find the peaks located at 3116 and 3334  $\text{cm}^{-1}$ , which are assigned to the  $-\text{NH}_2$  groups.<sup>[23]</sup> Besides the FT-IR results, the mass spectrometry also demonstrates the molecular structure of AASCN with the peak positions at 59.06 representing  $\text{AA}^+$  and 57.97 representing  $\text{SCN}^-$ . Combining the AASCN synthesis processes and characterization results analyzed earlier, the molecular structure of AASCN is supposed to be accurately confirmed.

We utilized a one-step spin-coating method with antisolvent to fabricate perovskite films in this work. The corresponding perovskite film formation process includes pre-annealing (nucleation and growth) and annealing (second growth). We applied a vapor treatment method to deposit AASCN on perovskite films after pre-annealing, which assures the AASCN plays a part in the second growth process of perovskite film. Figure 1b,c briefly illustrates the steps of the vapor treatment process and the diagram of molecular structure transition. This vapor treatment greatly weakens the Coulombic bondage between  $\text{AA}^+$  and  $\text{SCN}^-$  and fully releases the coordination activity of  $\text{AA}^+$  and  $\text{SCN}^-$ .<sup>[24]</sup> Unless stated otherwise, all "Treated" samples denote the perovskite film was prepared by 3  $\text{mg mL}^{-1}$  solution vapor treatment for 20 s. The effects of AASCN solution concentration and vapor treatment time on device performance are shown in Figures S4 and S5, Supporting Information. The corresponding parameters of devices are shown in Tables S1 and S2, Supporting Information. We applied FTIR spectra to certify the existence of AASCN on the perovskite film with the results shown in Figure 2a. In the intermediate state film that is with vapor treatment and without annealing, the characteristic peak of the  $\text{C}=\text{N}$  group is located at 1674  $\text{cm}^{-1}$ , and the new peak that appears at about 2079  $\text{cm}^{-1}$  is  $\text{SCN}^-$ , which both indicates the existence of AASCN.<sup>[15,25]</sup> After annealing, we found that only the  $\text{C}=\text{N}$  group

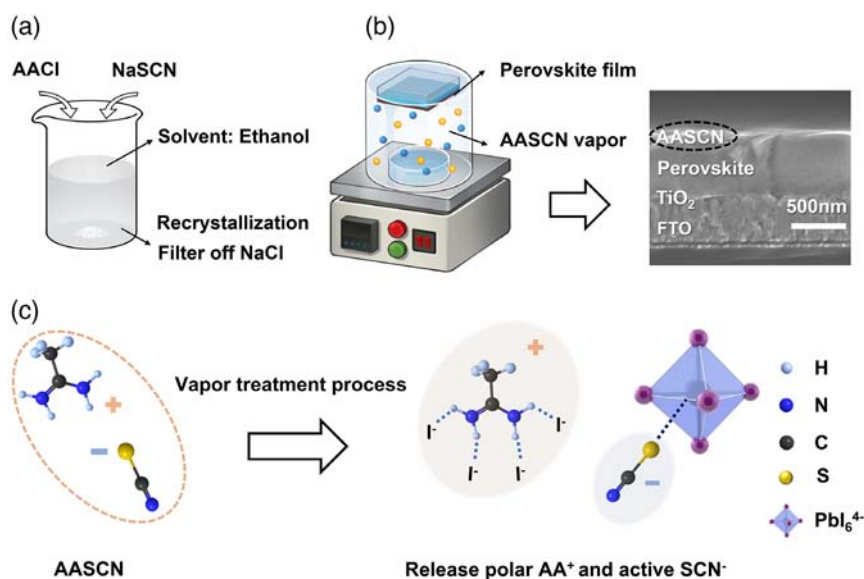


**Figure 1.** Schematic of acetamidine thiocyanate (AASCN) synthesis and vapor treatment process. a) Schematic diagram of AASCN synthesis. b) Simplified scheme of AASCN vapor treatment process and cross-sectional scanning electron microscope (SEM) images of the treated film. c) Diagram of molecular structure transition during the vapor treatment process. The orange dashed ellipse represents a weakened Coulombic bondage between  $\text{AA}^+$  and  $\text{SCN}^-$  and blue dashed straight lines indicate effective hydrogen bonds between  $\text{AA}^+$  and  $\text{I}^-$ .

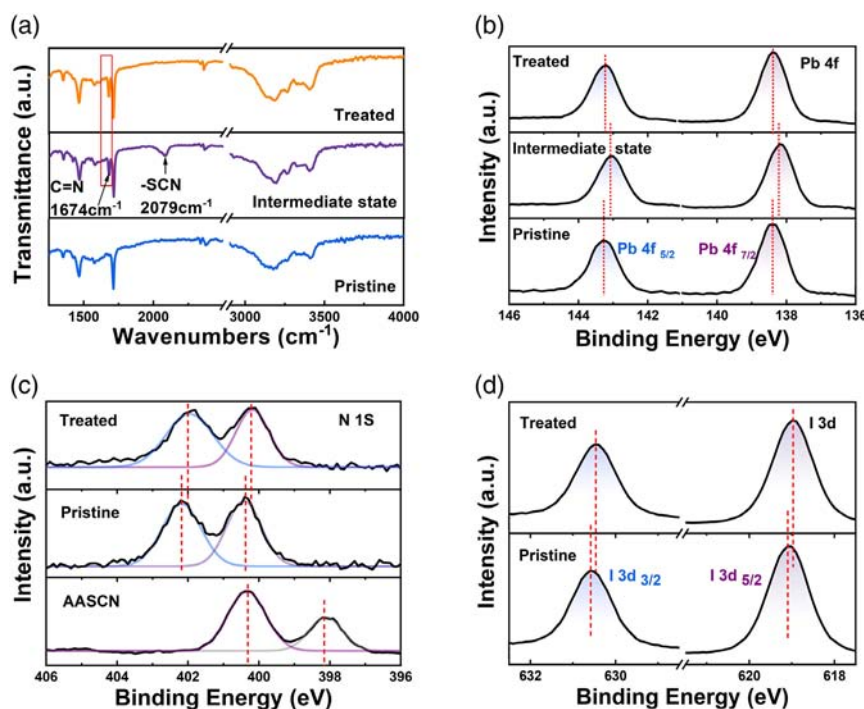


**Figure 2.** Characterization of existence and interaction of AASCN on perovskite film. a) Fourier transform infrared (FT-IR) spectra of pristine, during the treatment process and treated perovskite films. b–d) X-ray photoelectron spectrometer (XPS) spectra of Pb, N, and I of the perovskite films with and without treatment.

could be observed in the treated film, which may result from that the  $\text{SCN}^-$  escaped during the annealing.<sup>[26]</sup> Meanwhile, the  $\text{C}=\text{N}$  peak exhibits an observable shift of  $14\text{ cm}^{-1}$  for AASCN (Figure S2, Supporting Information) when incorporated with perovskite film, suggesting a strong interaction between AASCN and perovskite film.<sup>[27]</sup>

To further confirm the existence of AASCN and its chemical interaction with perovskite film, we applied X-ray photoelectron spectrometer (XPS) analysis. The full XPS spectra of the perovskite films are shown in Figure S6, Supporting Information, and Pb 4f spectra are shown in Figure 2b. Compared with pristine film, the Pb 4f<sub>5/2</sub> and Pb 4f<sub>7/2</sub> peaks exhibit a shift in the intermediate state, which may result from the coordination between  $\text{SCN}^-$  and Pb–I octahedrons.<sup>[22,28]</sup> After annealing, the Pb 4f peaks shift back to their original position, indicating that the  $\text{SCN}^-$  escaped during the annealing. The S 2p spectrum is shown in Figure S7, Supporting Information. There is no signal of S 2p in treated films, which is in accordance with the analyzed results of the Pb 4f peak. From the high-resolution N 1s spectrum of AASCN (Figure 2c), we can find that there are two peaks at 400.3 eV for the  $\text{C}=\text{N}$  group and at 398.2 eV for  $\text{SCN}^-$  group, respectively.<sup>[29,30]</sup> The N 1s XPS spectrum of pristine perovskite film is also shown in Figure 2c. The binding energy of 402.2 eV (light blue region) attributes to the N element in  $\text{MA}^+$ .<sup>[15]</sup> In the treated perovskite film, the N 1s peak of the  $\text{C}=\text{N}$  group shifts from 400.4 to 400.2 eV, and the peak of N in  $\text{MA}^+$  shifts from 402.2 to 402 eV. The binding energy shifts may result from the interaction of AASCN with perovskite.<sup>[31]</sup> Figure 2d shows the core-level spectra of I 3d. For the pristine film, the peaks located

at 630.5 and 619.1 eV are corresponding to I 3d<sub>3/2</sub> and I 3d<sub>5/2</sub>, respectively. Compared with pristine film, the I 3d<sub>3/2</sub> and I 3d<sub>5/2</sub> peaks shift to lower binding energies of 630.4 and 619.0 eV in the treated film. The peak shift of I 3d may come from the hydrogen bond of  $\text{H}\cdots\text{I}$  between  $\text{AA}^+$  and perovskite crystals.<sup>[28]</sup>

To investigate the influence of AASCN vapor treatment on the perovskite film crystalline property, scanning electron microscope (SEM) and X-ray diffraction (XRD) were carried out on perovskite films with and without treatment. The SEM images of the surface morphology of pristine and treated perovskite films are shown in Figure 3a,b with the grain size distribution shown in the inset. It is noted that some pinholes exist in the pristine film, and these pinholes have been effectively eliminated after treatment. In addition, the scattered white spots, which are assigned to  $\text{PbI}_2$  particles produced during the perovskite film formation, decrease significantly after treatment. The grain size distribution of the pristine perovskite film ranges from 0.2 to 0.8  $\mu\text{m}$  with a peak value of about 0.45  $\mu\text{m}$ . After AASCN vapor-treated, the average crystal grain size increases obviously and the distribution is more uniform located in the range of 0.3–1.0  $\mu\text{m}$  with a peak value of about 0.6  $\mu\text{m}$ . This phenomenon is attributed to the controlled secondary growth process of perovskite by introducing  $\text{SCN}^-$ . The  $\text{SCN}^-$  can partially decompose unstable small perovskite crystals due to its extraction effect, leading to fast and efficient de-nucleation.<sup>[32]</sup> In the Ostwald ripening mechanism, the dissolution/de-nucleation rate of unstable small perovskite crystals is critical to the growth of stable large perovskite crystals.<sup>[33]</sup> We propose that the introduction of

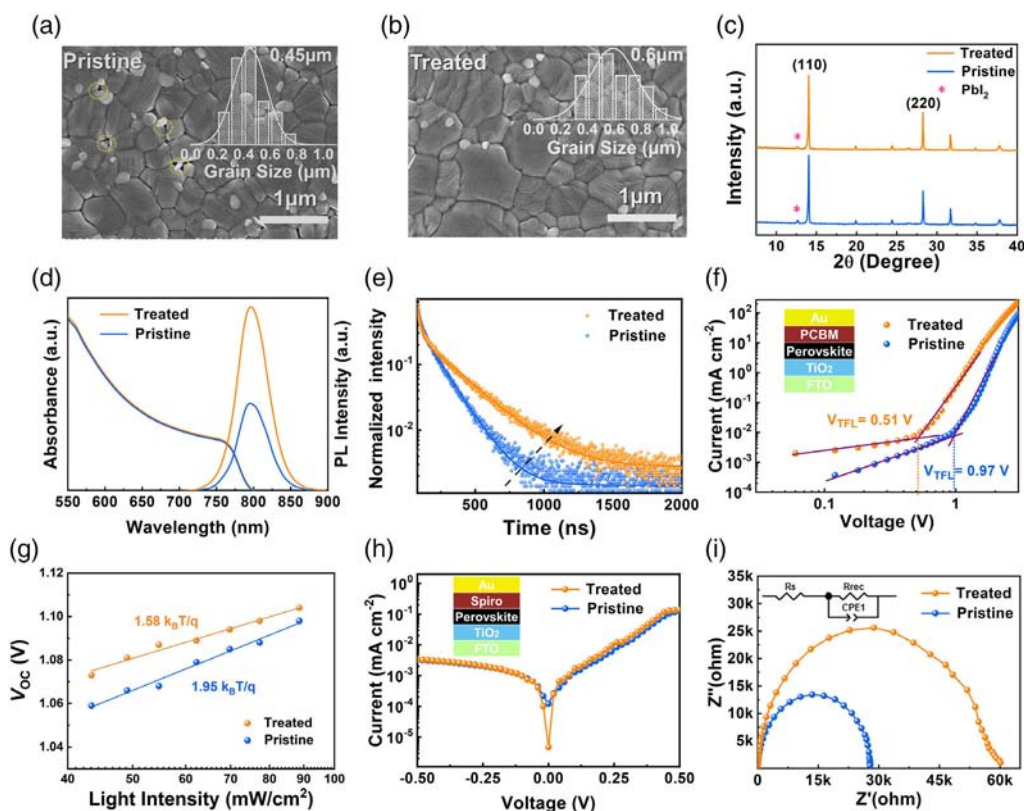


**Figure 3.** Characterizations of perovskite films with and without AASCN vapor treatment. a, b) SEM images of pristine and treated perovskite film. The inset presents the corresponding grain size distribution. c) XRD patterns. d) UV-vis absorption and steady-state photoluminescence (PL) spectra. e) Time-resolved PL (TRPL) spectrum of the pristine and treated films. f) Dark  $I$ - $V$  curves of the electron-only devices. g)  $V_{OC}$  of pristine and treated perovskite solar cells (PSCs) plotted against the logarithm of light intensity. h) Dark current curves of photovoltaic devices. i) Nyquist plots of perovskite solar cells.

$SCN^-$  increases the de-nucleation rate, further promoting the secondary growth of perovskite crystals.

Subsequently, the XRD patterns of perovskite films with and without treatment are shown in Figure 3c. The main peaks at  $13.98^\circ$ ,  $28.20^\circ$ , and  $31.81^\circ$  are characteristic peaks of perovskite, representing (110), (220), and (310) diffraction, respectively.<sup>[34]</sup> To investigate the influence of AASCN vapor treatment on residual  $PbI_2$  in perovskite, the peak ratio of  $PbI_2$ /perovskite from XRD was calculated. The peak ratio decreases from 0.087 to 0.073 after treatment, indicating a significant decrease in  $PbI_2$ . We also calculated the full width at half maximum (FWHM) of the perovskite (110) crystal plane to explore the crystallinity (Figure S8, Supporting Information). It is noted that the FWHM of the treated perovskite is 0.113, which is smaller than that (0.118) of the pristine sample, indicating enhanced crystallinity with AASCN vapor treatment. The absorption spectrum (Figure 3d) of the perovskite film with AASCN vapor treatment is almost the same as that of pristine perovskite thin film, indicating there is a negligible influence of vapor treatment on the perovskite film absorption.

To provide more insights into the influence of AASCN vapor treatment on the photoelectric qualities of the perovskite films, steady-state photoluminescence (PL) and time-resolved photoluminescence (TRPL) spectra were further conducted. The PL

results of perovskite films on glass substrates are shown in Figure 3d. In comparison with the pristine perovskite film, the SSPL intensity of treated perovskite film is obviously higher, indicating that the AASCN treatment process can reduce defect states.<sup>[35]</sup> Furthermore, as shown in Figure 3e, the average carrier lifetimes (Table S3 and Note S1, Supporting Information) of the treated film is 202.15 ns which is nearly two times higher than that (115.19 ns) of pristine film. The TRPL results further demonstrate the reduction of defects in the perovskite films resulting from the AASCN treatment.

The space charge limited current (SCLC) technology was employed to estimate the defect density of pristine and treated perovskite films. We fabricated electron-only devices with a configuration of FTO/TiO<sub>2</sub>/perovskite (AASCN)/PCBM/Au. As shown in Figure 3f, the trap-filled limit voltage ( $V_{TFL}$ ) value of the treated device decreases to 0.51 from 0.97 V of the pristine device. It is known that the trap density ( $N_t$ ) is related to  $V_{TFL}$  and can be calculated based on the following equation:  $N_t = (2\epsilon\epsilon_0 V_{TFL}) / (qL^2)$ , where  $L$  is the film thickness,  $\epsilon_0$  the vacuum permittivity,  $q$  the electron charge, and  $\epsilon$  the relative dielectric constant.<sup>[36]</sup> Thus, the trap density of the treated and pristine devices is calculated to be  $1.76 \times 10^{15}$  and  $3.35 \times 10^{15} \text{ cm}^{-3}$ , respectively. Compared with the pristine film, the lower trap density in the treated film indicates that the



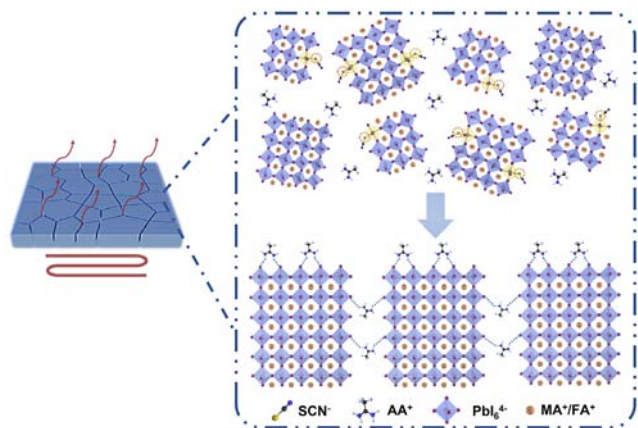


**Figure 4.** Detailed mechanism of AASCN dual-functional materials for secondary growth of perovskite film.

N–H bond of AA<sup>+</sup> can combine with I<sup>−</sup> and effectively reduce defects in the perovskite film. In addition, we gathered the  $V_{OC}$  of pristine and treated PSCs versus light intensity to calculate the ideality factor ( $n_{ID}$ ) according to the following equation

$$V_{OC} = \frac{n_{ID} k_B T}{q} \ln(I) \quad (1)$$

where  $k_B$  is the Boltzmann constant,  $T$  the thermodynamic temperature, and  $q$  the electron charge. From Figure 3g, the  $n_{ID}$  declines from 1.95 to 1.58 after the AASCN treatment, demonstrating that AASCN vapor treatment is effective in passivating the surface defects. We further applied dark current measurements to investigate the current leakage in devices with

the finding presented in Figure 3h. It is clear that the treatment can largely suppress the current leakage in devices. The electrochemical impedance spectroscopy (EIS) spectra of pristine and treated devices are shown in Figure 3i, and the corresponding fitting parameters are summarized in Table S4, Supporting Information. Obviously, the recombination resistance ( $R_{rec}$ ) of the treated device is almost two times higher than that of the pristine device, resulting from the reduction of trap states in the treated device.

According to the aforementioned results and previous related research, we propose a possible mechanism to synergistically achieve perovskite crystallization regulation and defects passivation by AASCN treatment. As shown in **Figure 4**, randomly oriented small-sized perovskite crystals are distributed in the pristine perovskite films after pre-annealing. During the AASCN vapor treatment, the vapor treatment process weakens the Coulombic bond between AA<sup>+</sup> and SCN<sup>−</sup>, releasing polar AA<sup>+</sup> and coordination-active SCN<sup>−</sup>. Because of its small size and high structural freedom, linear SCN<sup>−</sup> can interact with Pb–I octahedrons, and followed by an Ostwald ripening process, the small-sized perovskite recrystallizes into larger and oriented perovskite crystals at the perovskite second growth process. At the same time, the polar AA<sup>+</sup> contains four rotation-restricted C–N bonds, which improve the stability of the perovskite and effectively passivate the surface defect states through the N–H...I bond. We further explored the treatment depth in perovskite films via the time-of-flight secondary-ion mass spectrometry (ToF-SIMS) technique. ToF-SIMS depth profiles and the reconstructed 3D images are illustrated in Figure S9, Supporting Information. The ToF-SIMS depth profiles confirm this treatment can permeate through the perovskite film. Through recrystallization regulation by SCN<sup>−</sup> and defect passivation by AA<sup>+</sup>, the defect

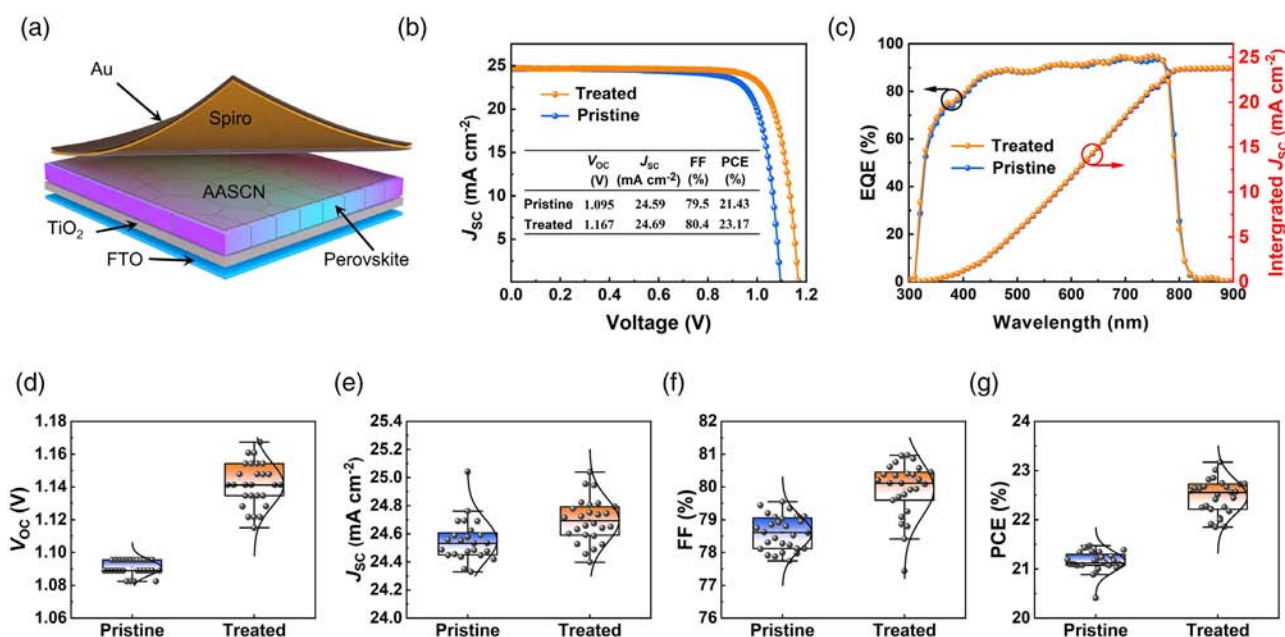


**Figure 5.** Device characteristics. a) Schematic illustration of PSC configuration. b) The best  $J$ – $V$  curves of pristine and treated devices. c) External quantum efficiency (EQE) spectra with integrated current densities of pristine and treated devices. d–g) Statistical distribution of the photovoltaic parameters for PSC devices: d) distribution of  $V_{OC}$ ; e) distribution of  $J_{SC}$ ; f) distribution of FF; g) distribution of PCE.

density of perovskite film is supposed to be effectively decreased, which helps to achieve an improved PSCs performance.

We fabricated devices with structures of FTO/TiO<sub>2</sub>/perovskite (AASCN)/spiro-OMeTAD/Au shown in Figure 5a. The best current density–voltage (*J*–*V*) curves of the pristine and treated devices are shown in Figure 5b. We can find that the photovoltaic performance of the treated device is significantly improved. In detail, compared to the pristine device, the PCE of the treated device increases from 21.43% to 23.17%, *J*<sub>SC</sub> from 24.59 to 24.69 mA cm<sup>-2</sup>, *V*<sub>OC</sub> from 1.095 to 1.167 V, and fill factor (FF) from 79.5% to 80.4%. The significant increment of *V*<sub>OC</sub> may result from the effectively suppressed surface defects and better matching of interfacial energy levels (Figures S10 and Note S2, Supporting Information). As shown in Figure S11, Supporting Information, the hysteresis of the treated device is slightly alleviated, mainly resulting from the reduction of trap states. The external quantum efficiency (EQE) and integrated current density results are presented in Figure 5c. The integrated current density of the pristine and treated device is 23.80 and 23.85 mA cm<sup>-2</sup>, respectively. Figure S12, Supporting Information, shows that the stabilized PCEs of PSCs with and without AASCN treatment are ≈22.9% and ≈21.3%, respectively. The distribution of device parameters is shown in Figure 5d–g, these results show that the treated device exhibits excellent reproducibility. The AASCN is incorporated into the perovskite through different approaches and shields a positive effect on device performance. (Table S5 and Note S3, Supporting Information). We further explored the influence of AASCN vapor treatment on the stability of unencapsulated pristine and treated devices stored at room temperature with ≈20% relative humidity for ≈500 h. As shown in Figure S13, Supporting Information, the treated devices obviously exhibit better stability compared to the pristine devices. The enhanced long-term stability is mainly benefited from the enhanced perovskite crystallinity and passivated defects.

### 3. Conclusion

In conclusion, we synthesized a new AASCN material by rationally combining the polar amine cation for defect passivation and pseudo-halide anion for crystallization regulation of perovskite films. By introducing the AASCN into the perovskite film during its secondary crystal growth, we have synergistically realized the defect passivation through hydrogen bonds formed by the N–H bonds of the polar cation AA<sup>+</sup>, and crystallinity improvement through controlled crystallization process by SCN<sup>-</sup>. As a consequence, a PCE of 23.17% for FA<sub>0.25</sub>MA<sub>0.75</sub>PbI<sub>3</sub> PSCs is achieved with AASCN, compared to the pristine PSCs of 21.43%. Our work provides a perspective and insight into multifunctional materials design and synthesization for perovskite defect management, which further inspired the feasible approach to achieve efficient PSCs and other optoelectronic devices.

### 4. Experimental Section

**Materials:** Methylammonium iodide (MAI, 99.5%), formamidinium iodide (FAI, 99.5%), spiro-OMeTAD (99.8%), and Li-bis(trifluoromethanesulfonyl)imide (Li-TFSI, 99.5%) were purchased from Xi'an Polymer Light Technology

Corp. Lead iodide (PbI<sub>2</sub>, 99.999%), FK209 (99.5%), titanium tetrachloride (TiCl<sub>4</sub>, 99.99%), acetamidine hydrochloride (99.9%) and sodium thiocyanate (99.9%) were purchased from Aladdin. *N,N*-dimethylformamide (DMF, 99.8%), dimethyl sulfoxide (DMSO, 99.8%), and chlorobenzene (CB, 99.9%) were purchased from Acros Organics (extra dry). All materials were used without further modifications.

**Synthesis of AASCN:** To synthesize AASCN, the same mole ratio of acetamidine hydrochloride and sodium thiocyanate was dissolved in an ethanol solution. Then the mixture was stirred for 2 h under 25 °C. After filtering off the white precipitated NaCl (XRD result is shown in Figure S14, Supporting Information), the mixed solution was centrifuged to retain the supernatant and then purified by recrystallization. The white-colored AASCN were collected, dried, and stored under a nitrogen atmosphere. The nuclear magnetic resonance (NMR) spectra of AASCN are shown in Supporting Information (Figures S15 and S16).

**Device Fabrication:** TiO<sub>2</sub> layer was prepared on the clean FTO substrate by a water bath deposition method. As-fabricated TiO<sub>2</sub> layer was further treated with UV–ozone for 15 min before perovskite film deposition. The perovskite precursor solution was prepared by mixing 0.25 mmol FAI, 0.75 mmol MAI and 1.08 mmol PbI<sub>2</sub> with 650 μL DMF and 100 μL DMSO. The perovskite film was spin-coated on top of the TiO<sub>2</sub> layer at 4000 rpm for 18 s. At the time of 12 s to the end, 0.9 mL of diethyl ether was quickly dropped as an antisolvent. For the pristine sample, the as-fabricated perovskite film was annealed at 60 °C until it converted into brownish-red. For the treated sample, the brownish-red perovskite film was firstly annealed at 100 °C for 1 min. Then, the perovskite film was put into the AASCN environment for 20 s. Finally, pristine and treated perovskite film was annealed at 130 °C for 20 min. The AASCN environment was generated by dropping AASCN solution (3 mg mL<sup>-1</sup> in IPA) onto a metal sheet and annealed at 100 °C for 1 min. Then, the spiro-OMeTAD solution was spin-coated on top of perovskite films at a speed of 4000 rpm for 30 s. For 1 mL spiro-OMeTAD solution, 70 mg spiro-OMeTAD powder was added into 1 mL chlorobenzene, 17.5 μL Li-TFSI, and 26.6 μL tbp were added as additives. Finally, a 70 nm Au electrode was evaporated on the films under a high vacuum.

**Characterization:** The SEM images were captured using a scanning electron microscope (HITACHI SU8100). XRD was using a Bruker D8 Advance X-ray diffractometer. The absorption spectra of perovskite films were obtained by UV-vis spectrophotometer (UV-2600). Fourier-transform infrared (FT-IR) spectra were performed on a Bruker EQUINX55 spectrometer. XPS of the perovskite films was carried out using ESCALAB250Xi, Thermo 21 Fisher Scientific. The steady-state PL (SSPL) and time-resolved PL (TRPL) spectra of perovskite films were measured using an Edinburgh PL 980 spectrometer. The EIS measurements were carried out in an electrochemical workstation (IM6ex, Zahner, Germany). Bruker ascend 400 Hz was used for <sup>13</sup>C NMR and <sup>1</sup>H NMR. 1260-6120 (Agilent) was used for mass spectra. The current density–voltage (*J*–*V*) characteristics of PSCs were obtained using a Keithley 2400 source meter under a simulated AM 1.5G spectrum. The EQE data were obtained using a QE-R quantum efficiency measurement system (Enli Technology). To characterize the treatment depth of perovskite films, ToF-SIMS were measured by ION-TOF GmbH. The surface potential of pristine and treated films were analyzed using FMNanoview 1,000 AFM.

### Supporting Information

Supporting Information is available from the Wiley Online Library or from the author.

### Acknowledgements

This work was primarily supported by National Natural Science Foundation of China (Grant nos. 52232008, 51972110, 52102245, and 52072121), Beijing Natural Science Foundation (2222076, 2222077), project of State Key Laboratory of Alternate Electrical Power System with Renewable Energy Sources (LAPS202114), Huaneng Group Headquarters

Science and Technology Project (HNKJ20-H88), the Fundamental Research Funds for the Central Universities (2020MS023, 2020MS028) and the NCEPU "Double First-Class" Program.

## Conflict of Interest

The authors declare no conflict of interest.

## Data Availability Statement

The data that support the findings of this study are available from the corresponding author upon reasonable request.

## Keywords

acetamidine thiocyanate, dual-functional material design, perovskite solar cells, recombination losses suppressing

Received: August 5, 2022

Revised: September 17, 2022

Published online: October 17, 2022

- [1] A. Agresti, A. Pazniak, S. Pescetelli, A. Di Vito, D. Rossi, A. Pecchia, M. Auf der Maur, A. Liedl, R. Larciprete, D. V. Kuznetsov, *Nat. Mater.* **2019**, *18*, 1228.
- [2] S. Yang, S. Chen, E. Mosconi, Y. Fang, X. Xiao, C. Wang, Y. Zhou, Z. Yu, J. Zhao, Y. Gao, *Science* **2019**, *365*, 473.
- [3] P. Cui, S. Qu, Q. Zhang, B. Liu, L. Yan, S. Du, X. Wang, H. Huang, J. Ji, M. Li, *Energy Mater.* **2021**, *1*, 1.
- [4] J. Chen, D. He, N. Park, *Sol. RRL* **2022**, *6*, 2100767.
- [5] D. Luo, R. Su, W. Zhang, Q. Gong, R. Zhu, *Nat. Rev. Mater.* **2020**, *5*, 44.
- [6] J. Chen, N. G. Park, *Adv. Mater.* **2019**, *31*, 1803019.
- [7] E. Aydin, M. De Bastiani, S. De Wolf, *Adv. Mater.* **2019**, *31*, 1900428.
- [8] X. Zheng, B. Chen, J. Dai, Y. Fang, Y. Bai, Y. Lin, H. Wei, X. C. Zeng, J. Huang, *Nat. Energy* **2017**, *2*, 1.
- [9] J. M. Ball, A. Petrozza, *Nat. Energy* **2016**, *1*, 1.
- [10] D. Luo, W. Yang, Z. Wang, A. Sadhanala, Q. Hu, R. Su, R. Shivanna, G. F. Trindade, J. F. Watts, Z. Xu, *Science* **2018**, *360*, 1442.
- [11] E. H. Jung, N. J. Jeon, E. Y. Park, C. S. Moon, T. J. Shin, T.-Y. Yang, J. H. Noh, J. Seo, *Nature* **2019**, *567*, 511.
- [12] K. Wang, Z. Jin, L. Liang, H. Bian, D. Bai, H. Wang, J. Zhang, Q. Wang, S. Liu, *Nat. Commun.* **2018**, *9*, 1.
- [13] Q. Jiang, Y. Zhao, X. Zhang, X. Yang, Y. Chen, Z. Chu, Q. Ye, X. Li, Z. Yin, J. You, *Nat. Photonics* **2019**, *13*, 460.
- [14] Y. Zhang, J. Chen, X. Lian, M. Qin, J. Li, T. R. Andersen, X. Lu, G. Wu, H. Li, H. Chen, *Small Methods* **2019**, *3*, 1900375.
- [15] C. Liu, S. Liu, Y. Wang, Y. Chu, K. Yang, X. Wang, C. Gao, Q. Wang, J. Du, S. Li, *Adv. Funct. Mater.* **2021**, *31*, 2010603.
- [16] R. Lin, J. Xu, M. Wei, Y. Wang, Z. Qin, Z. Liu, J. Wu, K. Xiao, B. Chen, S. M. Park, *Nature* **2022**, *603*, 73.
- [17] W. Hui, L. Chao, H. Lu, F. Xia, Q. Wei, Z. Su, T. Niu, L. Tao, B. Du, D. Li, *Science* **2021**, *371*, 1359.
- [18] J. Jeong, M. Kim, J. Seo, H. Lu, P. Ahlawat, A. Mishra, Y. Yang, M. A. Hope, F. T. Eickemeyer, M. Kim, *Nature* **2021**, *592*, 381.
- [19] Q. Jiang, D. Rebolgar, J. Gong, E. L. Piacentino, C. Zheng, T. Xu, *Angew. Chem.* **2015**, *127*, 7727.
- [20] P. Singh, R. Mukherjee, S. Avasthi, *ACS Appl. Mater. Interfaces* **2020**, *12*, 13982.
- [21] Y. Yang, W. Zhao, T. Yang, J. Liu, J. Zhang, Y. Fang, S. F. Liu, *J. Mater. Chem. A* **2021**, *9*, 23597.
- [22] B. Yu, J. Shi, S. Tan, Y. Cui, W. Zhao, H. Wu, Y. Luo, D. Li, Q. Meng, *Angew. Chem., Int. Ed.* **2021**, *60*, 13436.
- [23] H. Li, G. Wu, W. Li, Y. Zhang, Z. Liu, D. Wang, S. Liu, *Adv. Sci.* **2019**, *6*, 1901241.
- [24] H. Lu, Y. Liu, P. Ahlawat, A. Mishra, W. R. Tress, F. T. Eickemeyer, Y. Yang, F. Fu, Z. Wang, C. E. Avalos, *Science* **2020**, *370*, eabb8985.
- [25] F. Zhang, B. Cai, J. Song, B. Han, B. Zhang, H. Zeng, *Adv. Funct. Mater.* **2020**, *30*, 2001732.
- [26] H. Dong, Z. Wu, J. Xi, X. Xu, L. Zuo, T. Lei, X. Zhao, L. Zhang, X. Hou, A. K. Y. Jen, *Adv. Funct. Mater.* **2018**, *28*, 1704836.
- [27] A. Mauerer, *Secondary Structural Changes of Spray Dried Proteins With Fourier Transform Infrared Spectroscopy*, Shaker Verlag GmbH, Germany **2006**.
- [28] L. Yuan, H. Luo, J. Wang, Z. Xu, J. Li, Q. Jiang, K. Yan, *J. Mater. Chem. A* **2021**, *9*, 4781.
- [29] N. C. D. Nath, K. Yoo, J.-J. Lee, *RSC Adv.* **2018**, *8*, 17365.
- [30] Y. Zhang, J. Jiang, Y. Chen, *Polymer* **1999**, *40*, 6189.
- [31] D. Bi, X. Li, J. V. Milić, D. J. Kubicki, N. Pellet, J. Luo, T. LaGrange, P. Mettraux, L. Emsley, S. M. Zakeeruddin, *Nat. Commun.* **2018**, *9*, 1.
- [32] N. D. Pham, V. T. Tiong, D. Yao, W. Martens, A. Guerrero, J. Bisquert, H. Wang, *Nano Energy* **2017**, *41*, 476.
- [33] M. Yang, T. Zhang, P. Schulz, Z. Li, G. Li, D. H. Kim, N. Guo, J. J. Berry, K. Zhu, Y. Zhao, *Nat. Commun.* **2016**, *7*, 1.
- [34] I. E. Jacobs, A. J. Moulé, *Adv. Mater.* **2017**, *29*, 1703063.
- [35] Y. Guo, W. Sato, K. Shoyama, H. Halim, Y. Itabashi, R. Shang, E. Nakamura, *J. Am. Chem. Soc.* **2017**, *139*, 9598.
- [36] Y. Liu, J. Sun, Z. Yang, D. Yang, X. Ren, H. Xu, Z. Yang, S. Liu, *Adv. Opt. Mater.* **2016**, *4*, 1829.